THE UNIVERSITY OF WARWICK

warwickpublicationswrap

highlight your research

http://wrap.warwick.ac.uk/

Novel approach for health monitoring of earthen embankments

Utili S. [1], Castellanza R. [2], Galli A. [3], Sentenac P. [4],

1 School of Engineering
University of Warwick, UK
formerly at University of Oxford, UK

2 Department of Geology and Geotechnologies
Università Milano-Bicocca, Italy

3 Department of Structural Engineering
Politecnico di Milano, Italy

4 Department of Civil Engineering
University of Strathclyde, UK

ABSTRACT. This paper introduces a novel modular approach for the monitoring of desiccation-induced deterioration in earthen embankments (levees), which are typically employed as flood defence structures. The approach is based on the use of a combination of geotechnical and non-invasive geophysical probes for the continuous monitoring of the water content in the ground. The level of accuracy of the monitoring is adaptable to the available financial resources.

The proposed methodology was used and validated on a recently built 2 km long river embankment in Galston (Scotland, UK). A suite of geotechnical probes was installed to monitor the seasonal variation of water content over a two-year period. Most devices were calibrated in-situ. A novel procedure to extrapolate the value of water content from the geotechnical and geophysical probes in any point of the embankment is illustrated.

Desiccation fissuring degrades the resistance of embankments against several failure mechanisms. An index of susceptibility is here proposed. The index is a useful tool to assess the health state of the structure and prioritise remedial interventions.

1. Introduction

Earthen flood defence embankments also known as levees are long structures usually made of local material available at the construction site. In the UK, flood defence embankments are mainly made of cohesive soils: either clay or silt. Most of them were built before the development of modern soil mechanics in the eighteenth century (Charles, 2008). Due to their progressive aging, proper infrastructure condition assessment, based on sound engineering, is becoming increasingly important (Perry et al., 2001).

The formation of desiccation cracks in earthen embankments and tailing dams (Rodriguez et al., 2007) made of cohesive soils during dry seasons is detrimental to their stability. Desiccation is responsible for the onset of primary cracks which first appear at the surface, and then propagate downwards, and for so-called secondary and tertiary cracks (Konrad and Ayad, 1997). Desiccation induced failures are deemed to become increasingly important as progressively more extreme weather conditions are predicted by climatologists to take place worldwide (Milly et al, 2002). Allsop et al. (2007) provide a comprehensive list of the several failure modes that may take place in earthen embankments. Several potential failure mechanisms are negatively affected by the presence of desiccation cracks such as: deep rotational slides starting from the horizontal upper surface (Utili, 2013); shallow slides developing along the flanks (Aubeny and Lytton 2004; Zhang et al., 2005); erosion of the flanks by overtopping water (Wu et al., 2011) and/or wave action (D'Elisio, 2007); and internal erosion (Wan and Fell, 2004). In particular, the presence of cracks can substantially decrease the resistance of embankments with regard to overtopping and internal erosion which alone count for 34 and 28 percent respectively of all the embankment failures in the world (Wu et al., 2011).

Monitoring and condition assessment of flood defence embankments worldwide are mainly carried out by visual inspections at set intervals (Morris et al., 2007; Andersen et al.,

3

67   1999). In a few countries (e.g. the UK (Environment Agency, 2006), the Netherlands, the US)

68   guidelines exist to rate the health/deterioration of embankments on the basis of a prescribed

69   set of visual features. Unfortunately, this type of assessment is purely qualitative and relies

70   heavily on the level of training and experience of the inspection engineer. So, there is

71   consensus among experts on the fact that although visual inspection provides valuable

72   information, a meaningful and robust assessment of the fitness for purpose of earthen flood

73   defence embankments cannot rely entirely on visual inspection (Allsop et al., 2007). On the

74   other hand, intrusive tests (e.g. Cone Penetration test, piezocones, vane tests, inclinometers)

75   are impractical for the monitoring of long structures like embankments given the necessity of

76   performing tests in several locations to account for the typical high variability of the ground

77   properties. The same applies to standard geotechnical laboratory tests which involve time-

78   consuming retrieval and transportation of samples to the laboratory.

79   In this paper, a cost effective approach employing a suite of geotechnical and geophysical

80   probes is proposed for the long term monitoring of the variation of water content in the

81   ground and of the liability to desiccation induced fissuring. The methodology is simple,

82   modular (*i.e.* the level of sophistication/accuracy is a function of the financial resources

83   available), and it can be readily implemented by the authorities in charge of the management

84   of earthen flood defence embankments and tailing dams.

85

86   **2.   Conceptual framework**

87   The methodology here proposed is based on the assumption that water content can be

88   selected as a direct indicator of the occurrence of extensive fissuring in the ground as

89   suggested by Dyer et al., (2009) and Tang et al., (2012). The authors are aware that a lot of

90   research has been recently performed to successfully relate the onset of cracks to soil suction

91   (e.g. Shin and Santamarina, 2011; Munoz-Castelblanco et al., 2012b). However, as recently

92 well illustrated by Costa et al., (2013), the formation and propagation of cracks in cohesive

93 soils depends on several other factors too, such as the drying rate and the amount of fracture

94 energy involved in the crack propagation. Considering flood defence embankments, loss of

95 structural integrity (*i.e.* loss of the structure capacity to withstand the design hydraulic load)

96 occurs when desiccation fissuring progresses to the extent that an interconnected network of

97 cracks is formed rather than when surficial cracks first appear. Therefore the approximation

98 introduced in relating the loss of structural integrity to a threshold value of suction appears no

99 less important than the approximation introduced in relating it to a threshold value in terms of

100 water content. Moreover, the cost of monitoring suction in a long embankment for an

101 extended period of time is very significant with the extra burden of necessitating complex

102 installation and maintenance procedures for the probes needed to measure suction. These

103 reasons underpin the authors' choice of monitoring the ground water content.

104   The position of any point in a long linear structure like an embankment or tailing dam

105 can be defined according to either a global Cartesian coordinate system (X,Y,Z) or a local

106 coordinate system defined at the level of the structure cross-sections. For sake of simplicity,

107 the following choice was made: a curvilinear global coordinate, s, running along the

108 longitudinal direction of the structure which uniquely identifies the location of any cross

109 section; a local Cartesian coordinate, x, lying in the horizontal plane and perpendicular to the

110 s coordinate; and a vertical downward Cartesian coordinate, z, which can be thought of as

111 both a global and local coordinate. So, the water content, w, in a generic point of the earthen

112 structure is a function of these three spatial coordinates and of time: $w(x,s,z,t)$. A local

113 tangential coordinate s_t was also defined as shown in Figure 1b. The procedure proposed to

114 determine the function $w=w(x,s,z,t)$ in the whole embankment is based on the following

115 actions:

116   1)   measurement of the water content profile along a vertical line P of coordinate x_P, s_P at

117   any time and depth $w(x = x_P, s = s_P, z, t) = w_P(z,t)$;

118   2)   measurements in some selected cross-sections, located at $s = s_i$ (herein the subscript i

119   is an integer identifying the embankment cross-section considered), at some discrete

120   time points t_k (herein the subscript k is an integer identifying the time point

121   considered), of the function $w(x, s = s_i, z, t = t_k) = w_{i;k}(x,z)$;

122   3)   measurement by geophysical techniques of the water content at predefined time

123   points, t_k, along the entire embankment (*i.e.* for any value of s);

124   4)   evaluation by extrapolation of the water content in any point at any time: $w(x,s,z,t)$.

125   Once the water content function $w(x,s,z,t)$ is determined, an index quantifying the

126   susceptibility of any cross-section of the embankment to desiccation fissuring can be defined

127   and a map of susceptibility can be generated to identify the most critical zones of the

128   structure (see section 8). The map is useful to set priorities for intervention in the zones

129   requiring remedial actions.

130

131   **3.   Description of the site**

132   In 2007, the construction of an earthen flood defence embankment enclosing a floodplain

133   along the river Irvine to drain excess waters from the river during floods was completed in

134   Galston (Scotland, UK). The embankment is made of an uppermost layer (5-10 cm) of a

135   sandy topsoil below which lies a core of glacial till containing several boulders (Figure 1).

136   Grass roots do not extend beyond the topsoil. A typical cross- section is sketched in Figure

137   1b. Although the inclination of the flanks is rather uniform, the size of the flanks and of the

138   upper surface vary quite substantially along the longitudinal direction giving rise to a non-

139 negligible spatial variation of the geometry of the cross-sections which may have

140 consequences in terms of the spatial variation of the water content in the ground (see sections

141 6 and 7).

142

143
a)

144

145 *b)*
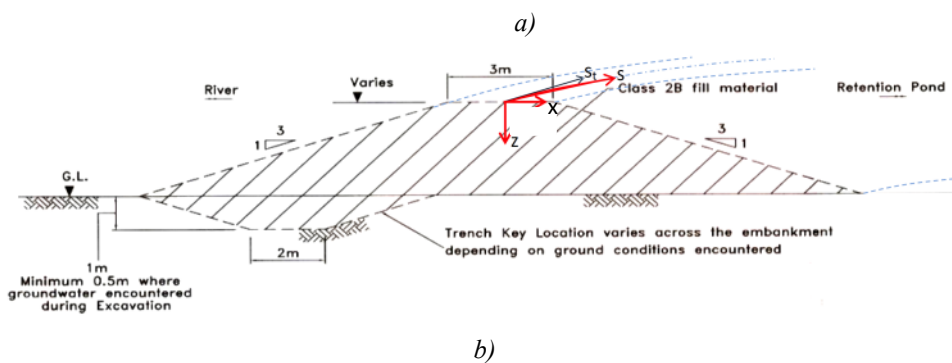
146 *Figure 1. a) Plan view of the monitored embankment; b) typical embankment cross section and system of*
147 *coordinates adopted in the paper.*

148

149 A number of standard geotechnical tests were carried out to characterise the ground

150 properties: measurements of gravimetric moisture content, void ratio, particle size

151 distribution and Atterberg limits were taken. The grain size distribution of both the top soil

152 and the glacial till was determined according to ASTM E11 (see Figure 2).
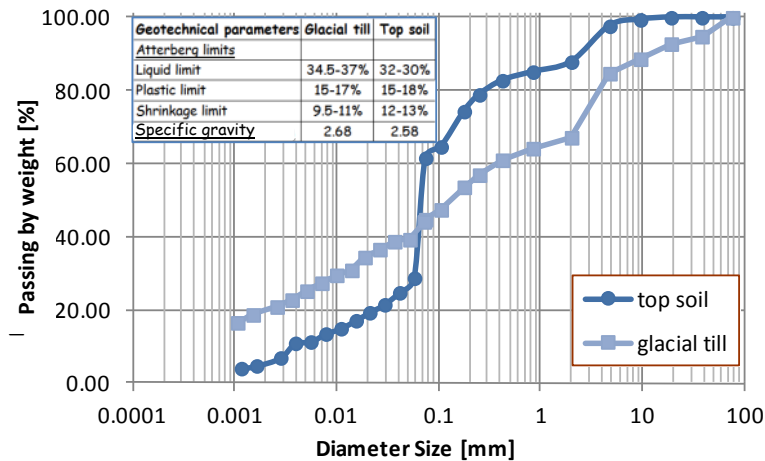
Figure 2. Particle size distribution of the glacial till and of the topsoil and main geotechnical indices.

4. Monitoring system

In the following, the main geotechnical and geophysical measurements of the monitoring system are described. The main technical features of all the probes employed in the monitoring programme (e.g. manufacturer, accuracy, operational range, etc.) are listed in Table 1.

4.1 Measurement of the water content along the selected vertical P

In Figure 3b, the vertical line P is plotted with the label PR2_E2. A data-logger, reading data at an hourly frequency was installed into a bespoke metallic fence close to the vertical line P (see Figure 3c). As schematically shown in Figure 3a and b, the following devices were connected to the data-logger:

a)   a theta probe (THP) made of four metal rods to be inserted in the ground to measure its water content at a depth of 25 cm. Special care was taken to avoid the formation of any air gaps between the prongs of the probe and the surrounding soil by prefilling the augered holes hosting the probes with a slurry and pushing the probe into undisturbed soil well beyond the hole bottom. The device takes a measurement of the relative

172   permittivity (also commonly called dielectric constant) of the ground which is then

173   converted into gravimetric water content;

174   b)   an equitensiometer (EQ) to measure suction up to a maximum value of 1000 kPa at

175   the same depth of 25 cm. This device consists of theta probe pins embedded into a

176   porous matric;

177   c)   a portable profile probe (PR), which is based on time domain reflectometry, to

178   measure the water content at six different depths from the ground surface (10, 20, 30,

179   40, 60 and 100 cm);

180   d)   two temperature probes inserted at 25 and 40 cm of depth in the ground.

181

182   **4.2 Measurement of the water content at cross-section A and B**

183   To evaluate the water content in the ground up to 1 meter of depth, several access tubes were

184   drilled into two cross-sections (A and B in Figure 3a and b) with the property of being

185   perpendicular to each other to better account for the influence of topographical orientation on

186   the measured water content (see section 7). Special care was taken to avoid the formation of

187   any air gaps between the tubes where the PR was inserted and the surrounding soil. Two

188   different instruments were employed:

189   a)   the PR, already described in the previous section, to measure the ground water content

190   along several vertical lines up to a depth of 1 m;

191   b)   a portable diviner (D) (see Sentek Diviner 2000 in table 1) to measure the ground

192   water content along various vertical lines every 10 cm from ground level down to 1.6

193   m of depth. This device is based on frequency domain reflectometry.

194   In section A, 10 access tubes were employed: 5 for the profile probe (labeled PR2_xx)

195   and 5 for the diviner (labeled DV_xx). In section B there were 12 measuring points: 6 for the

196   profile probe and 6 for the diviner. Some of the access tubes for the profile probe and the

diviner were laid down so as to be aligned along the longitudinal direction of the
embankment in order to perform a cross-comparison between them as it will be illustrated in
section 5 (see Figure 3a and b).

a)

b)
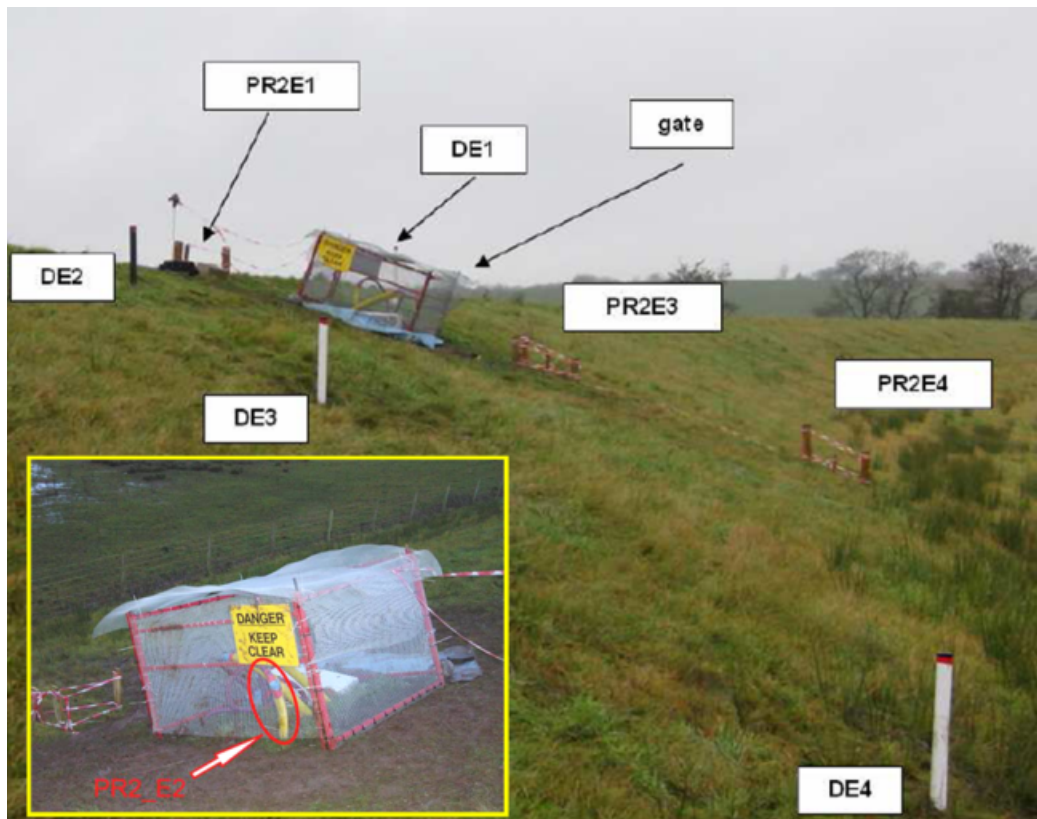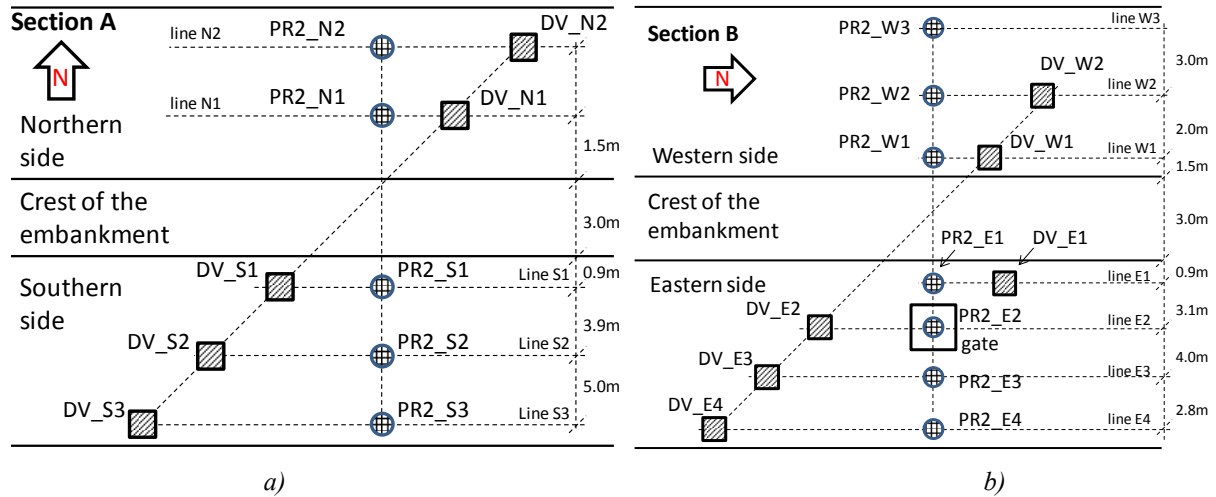
c)

*Figure 3. Position of the access tubes for the profile probe (PR2) and the diviner (D): (a-b) plan view of
sections A and B, respectively; (c) view of cross section B from the Eastern side.*

10

208   A weather station, manufactured by Pessl Instruments (see table 1), was installed 200m

209   south from section B of the embankment in order to collect data on rainfall precipitation, air

210   humidity, temperature and wind speed over the two year period of monitoring.

211

212   *Table 1. Main technical features of the probes employed in the monitoring.*

Device	Product name	Manufacturer	Accuracy and operational range
Equitensiometer	EQ2	Delta-T Devices Ltd United Kingdom www.delta-t.co.uk/	±10 kPa in the range from 0 to -100 kPa, ±5% in the range from -100 to -1000 kPa.
Theta probe	THP	Delta-T Devices Ltd United Kingdom www.delta-t.co.uk/	after calibration to a specific soil type: ±0.01 $m^3.m^{-3}$, in the range from 0 to 0.4 $m^3.m^{-3}$ with temperature from -20 to 40°C,
Profile probe	PR2	Delta-T Devices Ltd United Kingdom www.delta-t.co.uk/	after calibration to a specific soil type: ± 0.04 $m^3.m^{-3}$, in the range 0 to 0.4 $m^3.m^{-3}$ reduced accuracy from 0.4 to 1 $m^3.m^{-3}$
Diviner	Diviner 2000	Sentek Pty Ltd Australia www.sentek.com.au	+/- 0.003% vol in the range from -20 to +75°C
Weather station	iMETOS pro	Pessl Intruments http://metos.at/joomla/page/	temperature: +/- 0.1°C in the range -40° to +60° relative humidity: 1 % in the range 0 to 100% wind speed: 0.3 m/s in the range 0 to 60 m/s precipitation: +/- 0.1mm
Electromagnetic probe	CMD-2	Gf Instruments Czech Republic http://www.gfinstruments.cz	± 4% at 50 mS/m Operating temperature: -10 °C to +50 °C Maximum sampling rate: 10 Hz

213

214   **4.3 Geophysical measurements**

215   Electromagnetic surveys present the advantage of being non-intrusive and quick to be carried

216   out. Electromagnetic probes can measure the electrical conductivity of the ground. The

217   CMD-2 probe from Gf Instruments (see Table 1) was chosen for being a relatively cheap

218   device and simple to be used, *i.e.* without requiring a specific training. In Gf Instruments

219   (2011) the working principles of the device are illustrated. Measurements were taken by an

220   operator walking on the horizontal upper surface of the embankment along the longitudinal

221   direction at a constant pace of 5km/h, holding the CMD-2 approximately 1m above ground

222   with the device oriented perpendicular to the longitudinal direction so that the

223   electromagnetic flow-lines always lie in the plane perpendicular to the longitudinal direction

224   (*i.e.* the plane of the embankment cross-section).

11

225   Electrical resistivity tomography (ERT) is also a well-established geophysical technique

226   that is increasingly employed to measure electrical conductivity at the ground surface

227   (Munoz-Castelblanco et al., 2012a). Nowadays, 3D maps of in-situ water content can be

228   generated from ground resistivity measurements, as shown in (De Vita et al., 2012; Di Maio

229   and Piegari, 2011), once appropriate correlations between ground resistivity and in-situ water

230   content have been established. The potential for obtaining 3D maps of water content makes

231   ERT look like a very attractive tool for the monitoring of embankments. However, ERT

232   appears to be impractical for the continuous monitoring of an extended structure over long

233   timespans since it requires operators possessing the specialist skills to install the electrodes of

234   the devices in the ground and operate them. For this reason, in order to take geophysical

235   measurements of electrical conductivity in the embankment (see section 7.2) we chose to use

236   electromagnetic probes instead. Nevertheless, in the authors' opinion, ERT could still be

237   beneficially employed in the zones of the embankment identified as critical by the integrated

238   geotechnical/geophysical approach here proposed. In fact, ERT is useful to investigate in

239   great detail the state of fissuring of the ground in zones of limited extent.

240

241   **5.   Calibration of the geotechnical suite**

242   A key point of any monitoring system is the proper calibration of all the employed devices.

243   Regarding the calibration exercise undertaken, only the glacial till is of interest since the

244   thickness of the top soil in the embankment flanks, where all the measurements were taken, is

245   5 cm and the measurements were taken at depths always larger than 10 cm. A sequential

246   approach was adopted which is detailed in the following.

247

248   **5.1 Direct calibration of the theta probe**

249   The calibration curve for the theta probe (THP) was taken from Zielinski, (2009) (see Figure

250   4) who calibrated the THP using samples of till retrieved from the same quarry (Hallyards,

251   Scotland, UK) from which the till of our monitored embankment was extracted. The till was

252   retrieved from the quarry at five different known water contents and compacted into five

253   cylindrical containers with the same compaction effort as in the monitored embankment, *i.e.*

254   relative compaction of 95% with compaction control performed according to the

255   *Specification for Highway Works: Earthworks, Series 6000* (Highways Agency, 2006). Given

256   the high level of compaction and the non-swelling nature of this glacial till, the variations of

257   dry unit weight in the embankment over time and space occurring for the range of measured

258   in-situ water contents can be considered negligible (less than +/-5%). Hence, we transformed

259   the volumetric water contents measured by the geotechnical probes (profile probe, diviner,

260   etc.) into gravimetric water contents assuming the dry unit weight of the till at its optimal

261   water content, *i.e.* a maximum dry unit weight of 19.1 kN/m^3. This value was obtained as

262   average of 7 measurements performed in the laboratory on undisturbed U-38 samples

263   retrieved from the embankment. This value turned out to be almost identical to the value

264   measured by (Zielienski, 2011) on a small scale embankment built from the same glacial till

265   reconstituted in the laboratory.
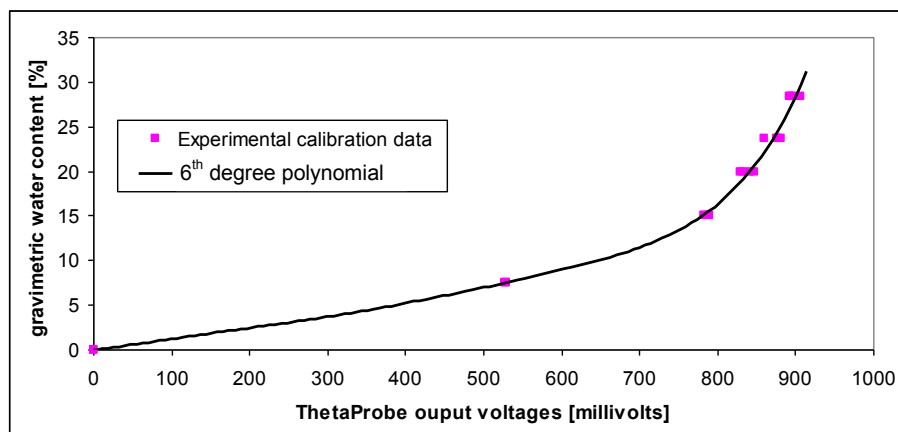
266

267   *Figure 4. Calibration curve for the theta probe; experimental calibration data after Zielinski (2009).*

13

268

5.2 Indirect calibration of the profile probe

270   The calibration of the profile probe (PR) was obtained by comparing the raw data in

271   millivolts obtained by the PR located at the gate in section B (PR2_E2 in Figure 3) at 20 and

272   30 cm depth with the measurements of the theta probe (THP) in the same location (20 cm

273   longitudinally away from the PR2_E2 in Figure 3) at 25 cm depth for a 4 month period. Data

274   were recorded every 4 hours. A strong similarity between the trends of the readings of the

275   two probes plotted in Figure 5 was observed. Since the two devices measure the water

276   content of the same portion of soil, a calibration procedure, based on the visual match of the

277   curves, was adopted: the scale of the ordinate axis of the THP readings (expressed in mV)

278   was varied until it satisfactorily matched the average (not reported in the figure to avoid

279   cluttering) of the two measurements at 20 and 30 cm depth obtained by the THP. The

280   resulting linear relationship between the values measured by the PR and the values measured

281   by the THP is shown in Figure 5. This relationship was used to convert the readings of the PR

282   into equivalent milliVolt units measured by the THP, and then they were in turn transformed

283   into gravimetric water content employing the calibration curve of the THP (Figure 4).

284
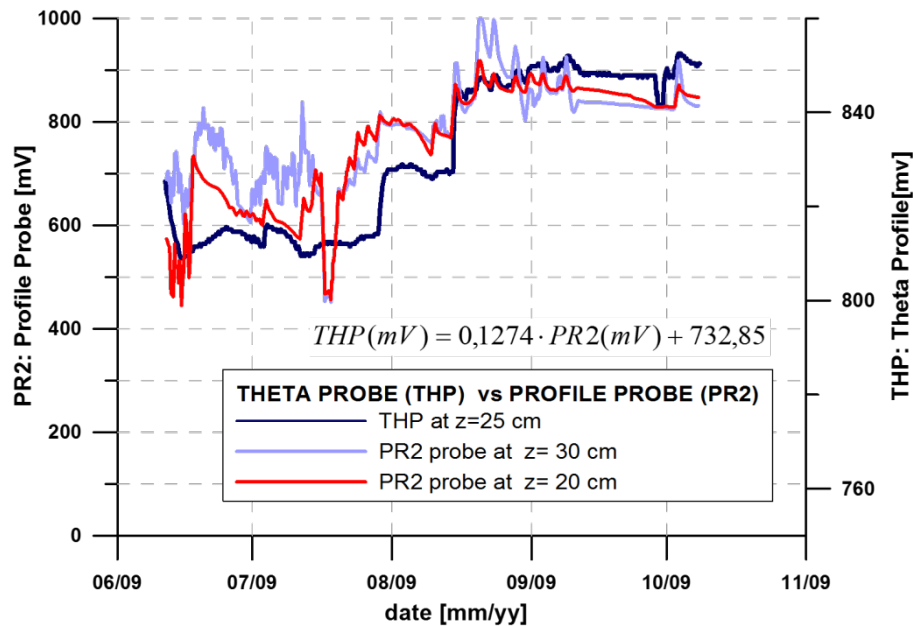
Figure 5. Calibration of the profile probe: measurements by the theta probe and the profile probe taken at the same location, PR2_E2 (see Figure 3).
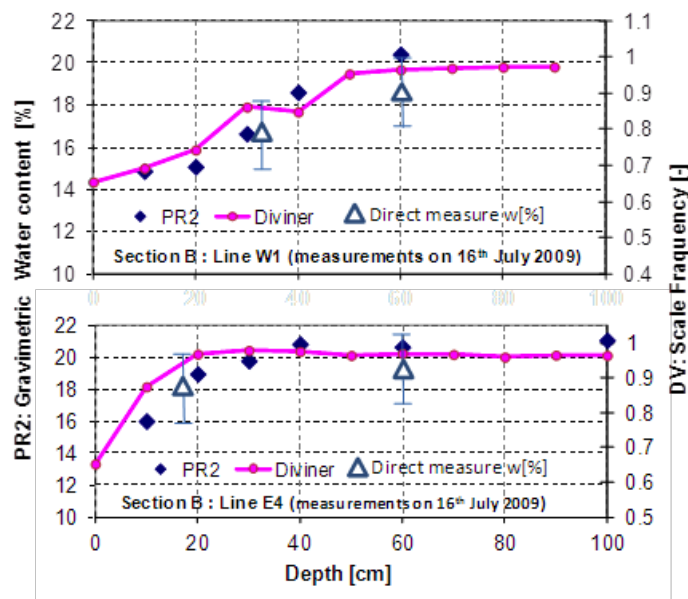
5.3 Indirect calibration of the diviner

Following the same approach described in the previous section, indirect calibration of the diviner (D) was performed by varying the scale of the frequencies measured by the D until a satisfactory match with the water content profile measured by the PR in the corresponding access tube was obtained. The corresponding PR access tube is the one aligned with the D tube in the longitudinal direction (e.g. DV_S3 and PR2_S3, see Figure 3a). In Figure 6a, two of the performed calibrations are shown. The curve shown in Figure 6b was obtained by repeating this procedure for all the monitoring points of the D in the time period considered.

Since the calibration procedures adopted for the PR and the D are based on cross-correlation, errors of measurement could be amplified. Hence, in order to check the amount of error amplification, direct measurements of the gravimetric water content were obtained via small in-situ samples taken in several points of the embankment on the same day (see the triangles in Figure 6a). Looking at Figure 6a, a good agreement between the values of water

15

302 content measured by the indirectly calibrated probes (PR and D) and direct measurements

303 emerges so that it can be concluded that error propagation is within acceptable limits.

304   Overall, the adopted calibration procedure has the obvious advantage of requiring only

305 small samples of soil for the direct calibration of the THP in the laboratory with the PR and D

306 indirectly calibrated in-situ. Conversely, direct calibration of the PR and D would require

307 retrieving large volumes of soil, to avoid the influence of boundary effects, at predefined

308 water contents to the laboratory.

309
310   *a)*
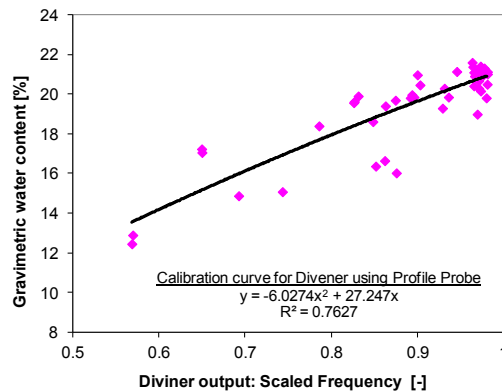
311
312   *b)*

313 *Figure 6. Calibration of the diviner by comparison with the measurements of the profile probe: a) examples of*
314 *cross comparisons for measurements taken in access tubes lying along the longitudinal line W1 and E4 (see Fig.*
315 *3 for location of the lines). The triangles with their error bar indicate the values of water content obtained via*
316 *direct measurement. b) Obtained calibration curve for the diviner.*

6.   Monitored data

In this section data relative to rainfalls, wind speed, relative humidity, air and ground temperature recorded by the weather station installed near to the embankment are analysed and compared with the ground water content recorded by the geotechnical suite in cross-sections A and B. The purpose of this analysis was first to establish the variation in time and space of the water content and secondly to identify correlations between weather variables and ground water content in order to separate out the variables significantly affecting the water content from the ones with a marginal influence which therefore can be discarded from the monitoring programme.

In principle it would be possible to calculate the effective amount of rainfall infiltrating in the ground from the calculation of evapotranspiration rates and the measurement or calculation of the amount of water runoff (Smethurst et al., 2012; Xu and Sing, 2001). However, the amount of runoff is likely to depend strongly on the inclination of the embankment flanks which varies locally and to a lesser extent on to the local vegetation cover. Moreover, a reliable estimate for a long linear structure with varying cross-section geometries would require several points of measurement. This is against the overall philosophy of the proposed methodology which aims to be as practical and simple as possible. Hence, we sought a relationship between in-situ water content and total precipitated rainfall. The latter can be measured directly by a nearby weather station. Furthermore, in the UK at least, weather stations can be found in several localities so that often there will be no need to install a new station in the site of interest. In summary, on one hand using total rainfall makes the correlation with the in-situ water content weaker because of the extra approximation of disregarding the variation of effective rainfall in the ground due to local lithological and geometrical variations; however on the other hand, it is far more desirable for

342   the authorities in charge of the monitoring system since total rainfall is much easier to be

343   ascertained.

344

6.1 Continuous measurements of water content profiles

346   Data were recorded over a 2 year period. Here, only an extract of two significant periods is

347   provided to illustrate the seasonal trends of desiccation and wetting of the embankment. The

348   most significant seasons are summer (see Figure 7) and winter (see Figure 9). In Figure 7a,

349   the ground water content profile is plotted together with the recorded daily rainfall

350   precipitation. Precipitations larger than about 5mm/day or reaching 5mm over a period of

351   consecutive daily rainfalls lead to noticeable increases of water content apparent in the spikes

352   of the curves relative to the water contents measured at 10 and 20 cm depth. No significant

353   variations of water content were ever recorded at depths larger than 60 cm.

354   In the upper part of Figure 7a, the suction measured by the EQ2 at 25 cm depth is

355   plotted. It emerges that the suction is well related to the rainfall records as well as to the

356   variation of water content. After several consecutive days of rainfall in late August, the

357   suction vanished to 0 for the entire winter period. For this reason, the variation of suction was

358   not reported in Figure 9b relative to the winter period. The THP measured water content at

359   the same depth of the suction measurements of the EQ in a point 15 cm away along the

360   horizontal direction so that an in-situ suction-water characteristic curve (SWCC) for the

361   considered point (PR2_E2) can be obtained (curve C in Figure 8). Zielienski et al. (2011)

362   measured in the laboratory the SWCC of this glacial till with different techniques (curves A

363   in Figure 8) and the SWCC (curve B in Figure 8) in a small scale embankment made of the

364   same material. In Figure 8, all these curves are plotted. Comparing the curves, it emerges that

365   the values of in-situ suction measured by the EQ lie close to the SWCC curves obtained in

18

366   the laboratory and also that the boundaries of the hysteresis cycles are close. This result is

367   quite remarkable.

368   Examining the recorded temperatures of the air and ground, a clear correlation between

369   the two is found: in Figure 7b the average between the maximum and minimum daily air

370   temperature turns out to be very close to the ground temperature at 10 cm depth. Relative

371   humidity and wind speed were rather constant during the monitored period (see Figure 7c).

372

373

374   *a)*

375

376   *b)*

19

c)
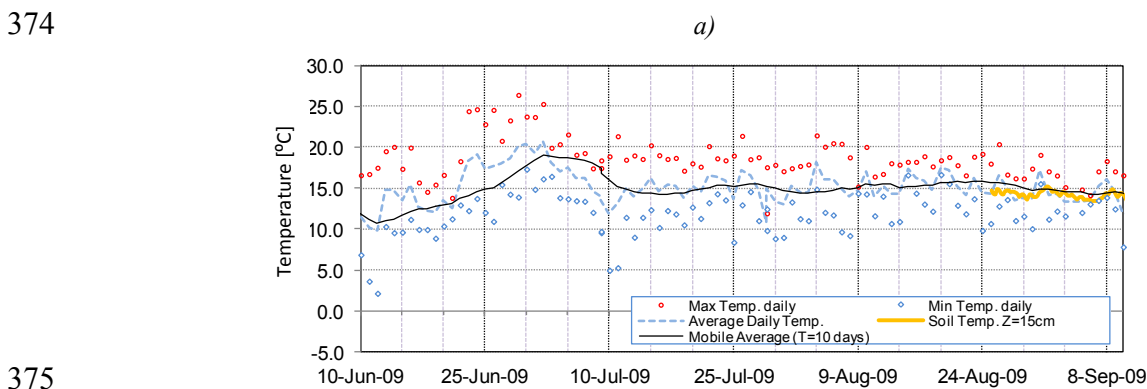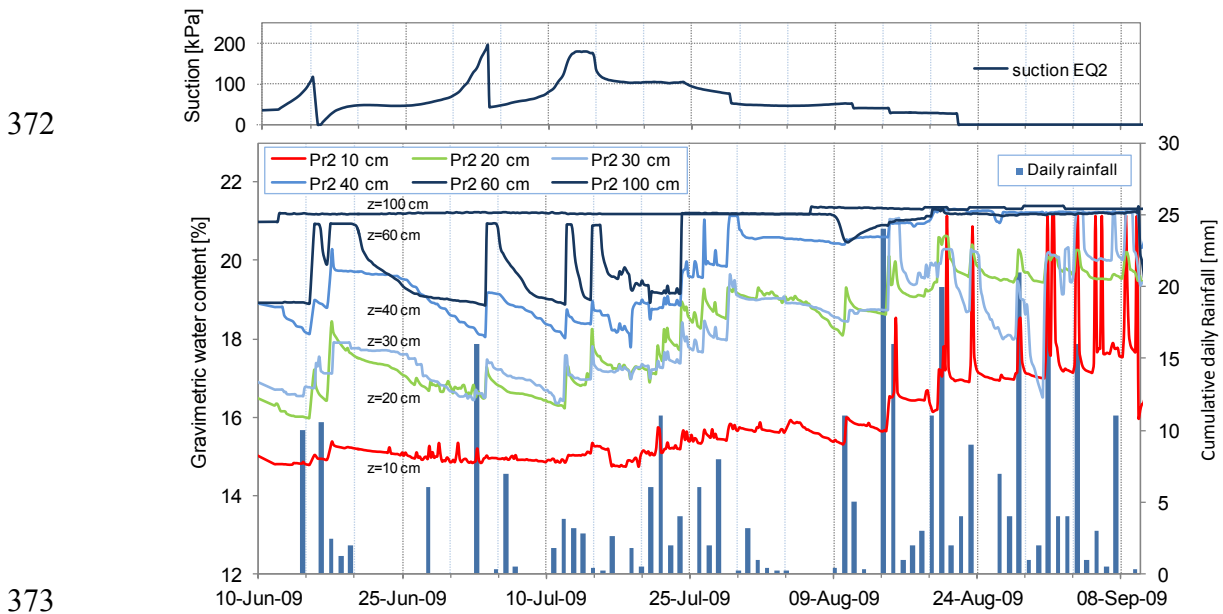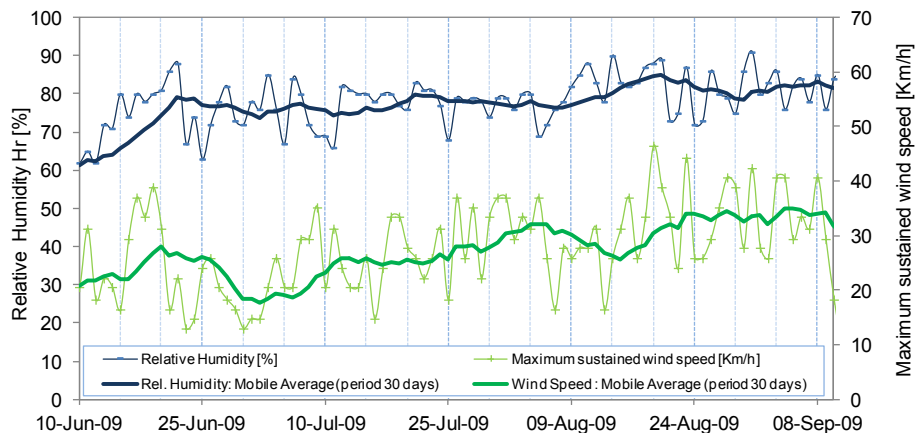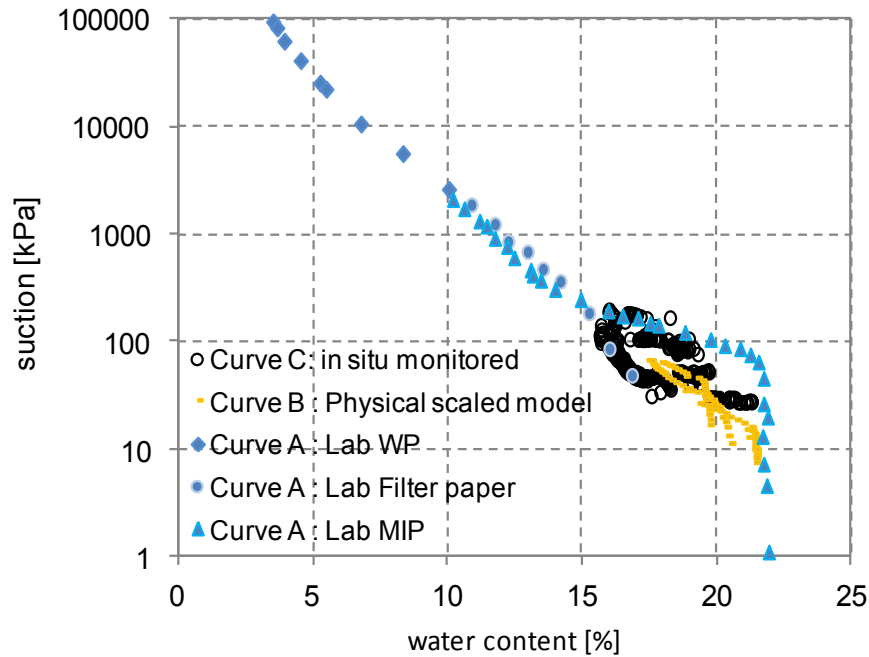
Figure 7. Summer 2009 (section B): a) evolution of the gravimetric water content, suction and rainfall record; b) average between the maximum and minimum daily air temperature (grey line) and ground temperature measured at 10cm depth; c) relative humidity and wind speed: the thin line follows the daily variation whereas the thick line is the mobile average over 10 days.

389

390   In winter (see Figure 9), higher precipitations take place leading to significantly larger

391   quick increases of the ground water content, in particular at shallow depths (10 cm). The

392   same remarks as for the summer period can be made with the exception of the wind speed

393   which varies significantly more than during the summer period.

394   From the monitored data, it can be concluded that the ground water content is highly

395   sensitive to the amount of total precipitation and to the length of the dry periods whereas no

396   significant correlation to relative humidity or to the variation of wind speed was found. These

397   observations lead to state that in principle it is possible to estimate the water content in a

398   cross-section, and in turn the cross-section susceptibility to desiccation fissuring (see section

399   8), from knowledge of both ground water content at the initial time of monitoring and

400   historical rainfall records. Given the limited resources available in this project, continuous

401   measurements in time are available only in 1 section of the embankment which is too little to

402   validate a reliable correlation between historical rainfall records and water content. However

403   in light of the results obtained here, we suggest that if a sufficient number of sections are

404   instrumented, a reliable correlation may be established so that meteorological data (especially

405   rainfall records) could be used to infer the amount of water content along the entire

406   embankment at any time according to the methodology presented in the next section (section

407   7) and to monitor susceptibility of the structure to desiccation fissuring (as expounded in

408   section 8). This methodology would have the advantage of not requiring periodic walk-over

409   surveys, but only the presence of a weather station nearby the structure.
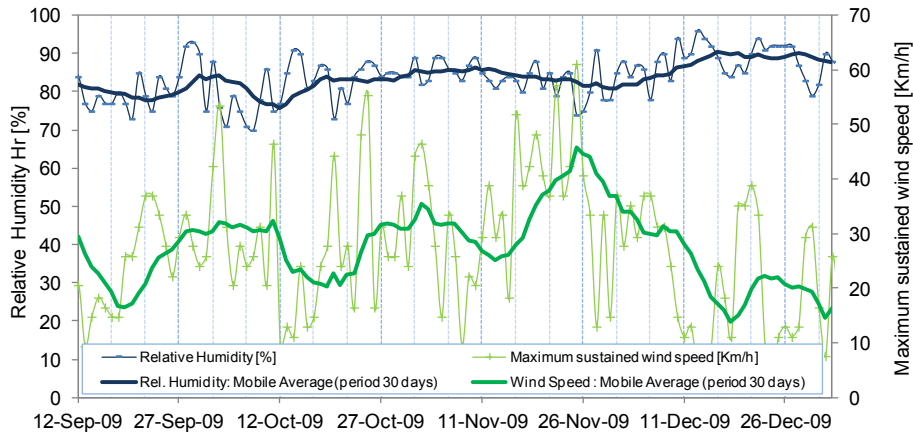
410

411

a)

412

413

b)

414

22

c)
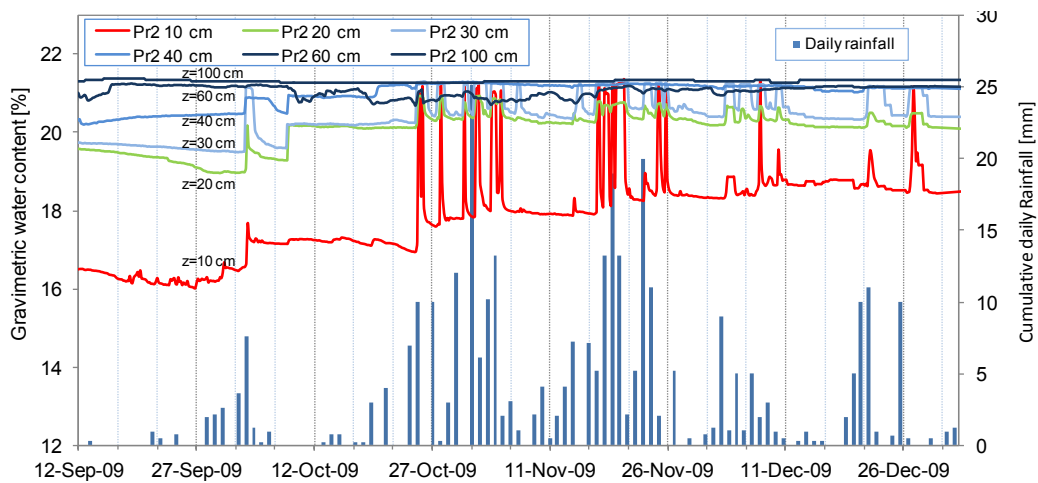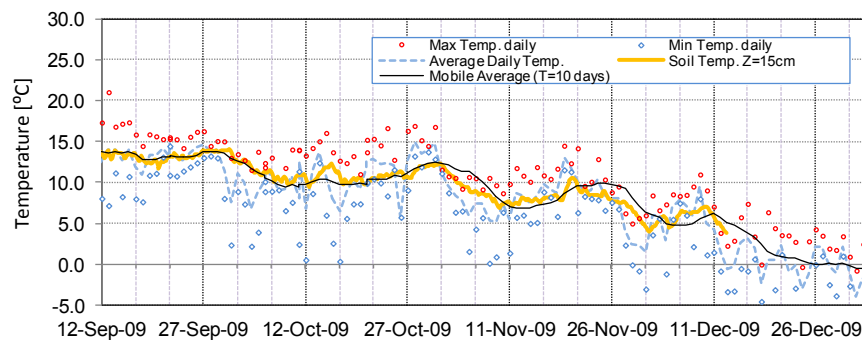
Figure 9. Winter 2009 (cross-section B): a) evolution of the gravimetric water content and rainfall record; b)
average between the maximum and minimum daily air temperature (grey line) and ground temperature
measured at 10cm depth; c) relative humidity and wind speed: the thin line follows the daily variation whereas
the thick line is the mobile average over 10 days.

6.2 Time discrete measurements of water content profiles

To evaluate $w_{i;k} = w(x,z) = w(x, s = s_i, z, t = t_k)$, measurements were taken from the profile

probe (PR) and the diviner (D) up to a depth of 1m (see Figure 10). In Figure 11a and Figure

11b, the evolution of the water content over time is plotted for section A and B respectively.

These figures were obtained by interpolating in space the values of water content measured

from the locations of the monitoring points (see Figure 3). The analyzed domain consists of

the uppermost 1 m of the cross-sections since no significant variations of water content were

ever observed at larger depths (see Figure 7 and Figure 9). To generate the plotted contours

of water content, first a mesh was created whose nodes coincide with the locations of the

readings taken from the PR and the D, then a post-processing FEM software, called GID

(GID, 2014), was employed to interpolate the values along the x and z coordinates. The

interpolation was repeated for measurements taken at different times (see Figure 11). From

these data it emerges that the water content varies significantly between the two sections. The

dependence of the water content on the geometrical alignment of the cross-sections, has been

23

436   accounted for in deriving the function $w(x,s,z,t)$ as it will be illustrated in the next

437   paragraph.

438

439   *a)*   *b)*
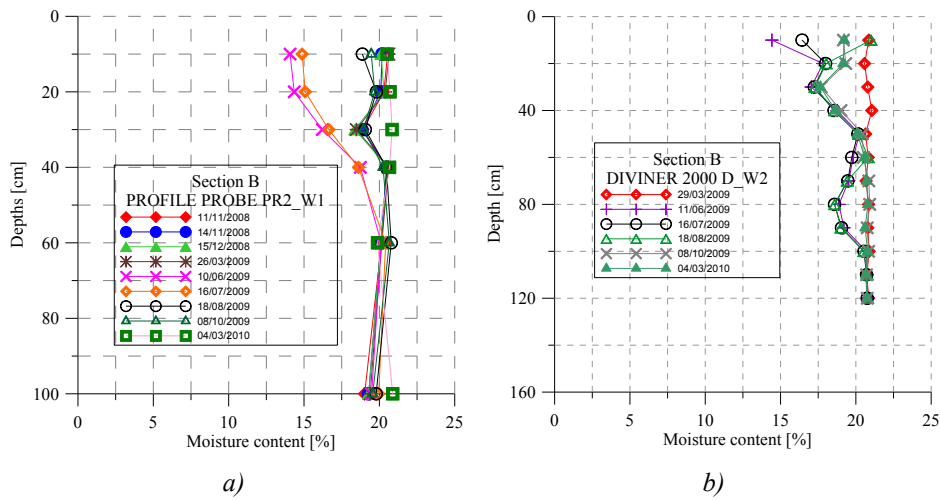
440   *Figure 10. Examples of profiles of the water content at different times in cross-section B: a) obtained by the*
441   *profile probe; b) obtained by the diviner.*

442

443   *a)*

444

24

445
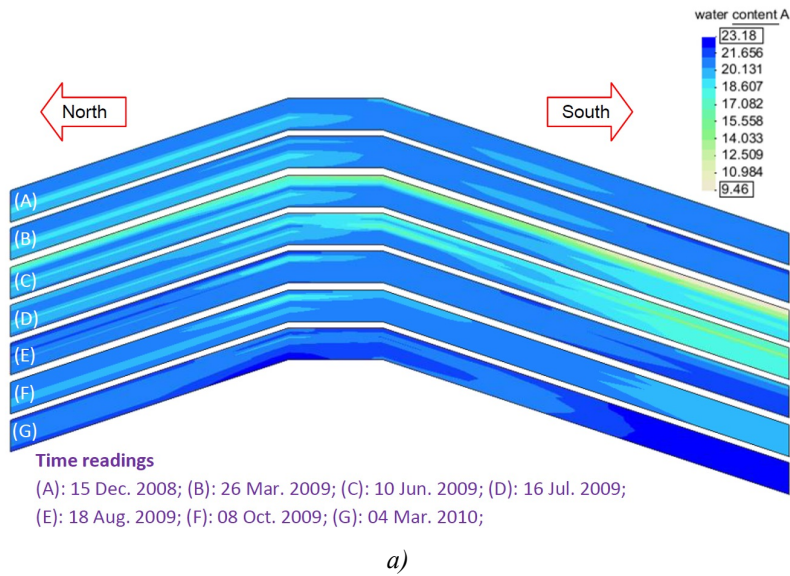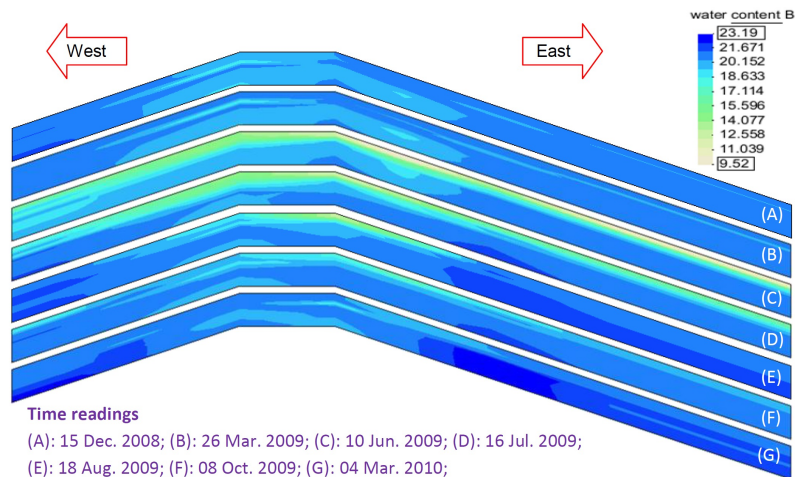
446 *Figure 11. Contours of the water content at different times over a period of 1.5 years: a) in cross-section A; b)*
447 *in cross-section B.*

448

449   7.   Extrapolation of the water content function for the entire structure

450 In the following, $w(x,s,z,t)$ will be derived first on the basis of data gathered by the

451 geotechnical suite only, secondly employing measurements of electrical conductivity taken

452 by the CMD-2 probe as well.

453

454 **7.1 Derivation of the water content function from the data retrieved by the geotechnical**

455 **suite**

456 In Figure 11, the water content of the two monitored cross-sections (A and B) is plotted. The

457 water content in any other cross-section is different due to two main factors:

458 (i)   different exposure to weather conditions (e.g. sunlight, rainfall and wind) which is a

459   function of the local orientation of the considered cross-section with respect to North.

460   This factor affects the ground water content along the flanks of the embankment much

461   more than underneath the horizontal upper surface.

462 (ii)   spatial variation of the geometrical, hydraulic and lithological properties of the cross

463   sections along the longitudinal coordinate s. Heterogeneities in the compaction

464   processes during construction, for example, are likely to cause a non-negligible spatial

465   variation of the hydraulic conductivity along the longitudinal direction. Concerning

466   compositional or lithological variability, this is likely to be small for the embankment

467   examined here due to the fact that it is made of homogeneous material and its young

468   age. However, in general, old earthen embankments are very often highly

469   heterogeneous comprising a mixture of several materials locally available at the time

470   of construction.

471   Regarding factor (i), considering the axis of symmetry of the cross-section (axis z in Figure

472   1a), exposure to each single weather element (e.g. wind, sunrays, rainfall droplets, etc.) gives

473   rise to a variation of water content which is either anti-symmetrical or nil in the case of equal

474   exposure (e.g. no wind and vertical sunrays), but the combination of the single weather

475   elements, *i.e.* the sum of the anti-symmetrical variations of water content due to exposure to

476   wind, exposure to sunrays, etc., may give rise to a non-negligible symmetrical variation of

477   water content as well. The anti-symmetrical part is a function of the orientation of the cross-

478   section considered whereas the symmetrical one is a function of the longitudinal coordinate *s*.

479   Regarding factor (ii), geometrical, hydraulic and lithological variations in the embankment

480   imply a variation of water content which in authors' opinion is much larger along the

481   longitudinal coordinate *s* than within each single cross-section and therefore is mainly

482   symmetrical. In summary, the water content variation in the embankment depends on both

483   cross-section orientation and cross-section position. The latter is expressed by the

484   longitudinal distance from a reference cross section (coordinate *s*). To better account for the

485   variation of water content due to these geometrical factors, cross-section orientation and

486   cross-section position, it is convenient to split the water content function, $w(x,s,z,t)$, into two

487   parts, a symmetrical, w^s, and an anti-symmetrical one, w^a, with respect to the axis of

488   symmetry of the cross-section:

489    $$w^s(x,s,z,t) = \frac{w(x,s,z,t) + w(-x,s,z,t)}{2} \quad \text{and} \quad w^a(x,s,z,t) = \frac{w(x,s,z,t) - w(-x,s,z,t)}{2} . \quad (1)$$

490   To account for the influence of cross-section orientation, it is convenient to employ a

491   function $\theta(s)$, with θ being the angle between s_t, direction normal to the cross-section, and a

492   reference direction here chosen as the geographical North (see Figure 12a). Considering

493   measurements of water content at discrete time points t_k, $w^a{}_k(x,s,z) = w^a(x,s,z,t=t_k)$ can be

26

494   expressed   as   the   weighted   average   of   the   values   of   water   content,

495    $w^a_{i;k}(x,z) = w^a(x,s=s_i,z,t=t_k)$, recorded at $t = t_k$ in the N instrumented cross-sections:

496    $$w^a_k(x,s,z) = w^a(x,s,z,t=t_k) = \sum_{i=1}^{N} w^a_{i;k}(x,z) \cdot \alpha_i(\theta)$$

(2).

497   with $\alpha_i(\theta)$ being weight functions accounting for the anti-symmetrical water content

498   variation in the embankment. The simplest choice for $\alpha_i(\theta)$ is to consider a linear

499   interpolation between the values of water content measured at the N instrumented sections as

500   illustrated in Figure 12c, so that:

501
$$\alpha_i(\theta) = \begin{cases} 1 & \text{for} & \theta = \theta_i & \forall i \in [1,..N] \\ 0 & \text{for} & \theta = \theta_{j \neq i} & \forall i,j \in [1,..N] \\ 1 - \dfrac{(\theta - \theta_i)}{(\theta_{i+1} - \theta_i)} & \text{for} & \theta_i \leq \theta \leq \theta_{i+1} & \forall i \in [1,..N] \\ 1 + \dfrac{(\theta - \theta_i)}{(\theta_{i-1} - \theta_i)} & \text{for} & \theta_{i-1} \leq \theta \leq \theta_i & \forall i \in [1,..N] \end{cases}$$

(3)

502   In general, it is advisable to instrument cross-sections forming equal angles between them so

503   that all the weight functions have the same periodicity in θ. Two sections are suggested as the

504   minimum number required for the procedure to work.

505   Analogously, with regard to the symmetrical part of the water content variation,

506    $w^s_k = w^s(x,s,z,t=t_k)$ is obtained as the weighted average of the values of water content,

507    $w^s_{i;k} = w^s(x,s=s_i,z,t=t_k)$, recorded in the N instrumented cross-sections at $t=t_k$:

508
$$w^s_k(x,s,z) = w^s(x,s,z,t=t_k) = \sum_{i=1}^{N} w^s_{i;k}(x,z) \cdot \beta_i(s)$$

(4)

509   with $\beta_i(s)$ being weight functions that depend on s rather than θ. Considering again a linear

510   interpolation between the values of water content measured at the N instrumented sections as

511   illustrated in Figure 12d, $\beta_i(s)$ are here defined as:

27

$$\beta_i(s) = \begin{cases} 1 & \text{for} & s = s_i & \forall i \in [1,..N] \\ 0 & \text{for} & s = s_{j \neq i} & \forall i, j \in [1,..N] \\ 1 - \dfrac{(s - s_i)}{(s_{i+1} - s_i)} & \text{for} & s_i \le s \le s_{i+1} & \forall i \in [1,..N] \\ 1 + \dfrac{(s - s_i)}{(s_{i-1} - s_i)} & \text{for} & s_{i-1} \le s \le s_i & \forall i \in [1,..N] \end{cases} \qquad (5)$$

512

513 Unlike the case of the α_i functions, for $0 \le s \le s_1$, β_1=1 whilst for $s_N \le s \le L$, β_N=1 with L

514 being the total length of the embankment. This means that for $0 \le s \le s_1$,

515 $w^s(x,s,z,t=t_k) = w^s(x,s=s_1,z,t=t_k)$ whilst for $s_N \le s \le L$, $w^s(x,s,z,t=t_k) =$

516 $= w^s(x,s=s_N,z,t=t_k)$. This is because in the regions $0 \le s \le s_1$ and $s_N \le s \le L$, there is only

517 water content measurements are available only for 1 section so that no interpolation can be

518 carried out. Obviously in the choice of the location of the 1st and N^{th} cross-sections, care

519 should be taken to minimise the length of the longitudinal segments $s_1 - 0$ and $L - s_N$.

520
521 *a)* *b)*

522
523 *c)* *d)*
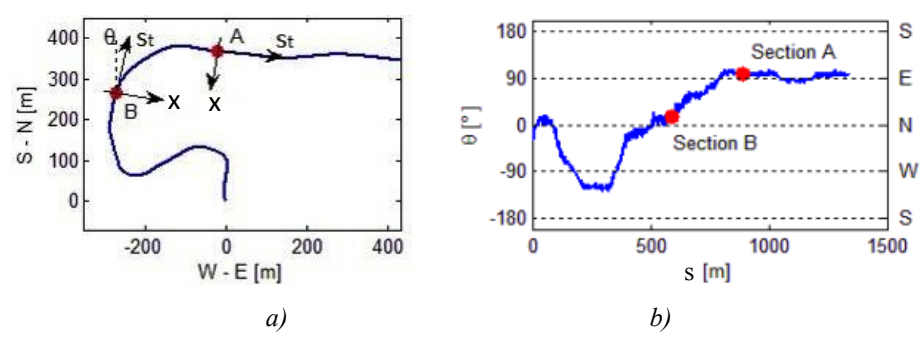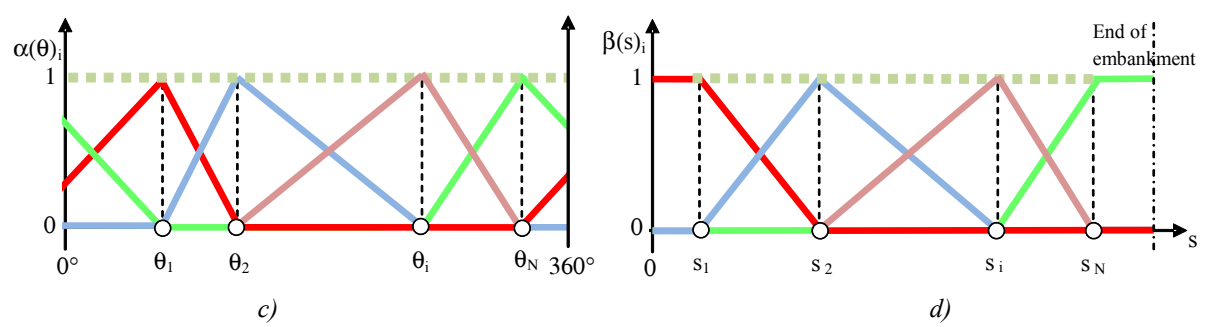
524 *Figure 12. (a) plan view of the embankment layout; (b) orientation of the longitudinal axis of the embankment*
525 *with respect to the North; c) α weight functions against cross-section orientation; d) β weight functions against*
526 *longitudinal coordinate s.*

527

528   The water content in any point of the embankment can now be obtained substituting Eqs.

529 (3) and (5) into Eq. (1):

530 $$w_k(x,s,z) = w(x,s,z,t=t_k) = \sum_{i=1}^{N} w_{i;k}^a(x,z) \cdot \alpha_i(\theta) + \sum_{i=1}^{N} w_{i;k}^s(x,z) \cdot \beta_i(s)$$

(6)

531 In our case $N=2$, so that $w_k(x,s,z)$ is calculated as:

532 $$w_k(x,s,z) = w(x,s,z,t=t_k) = w^a(x,s=s_1,z,t=t_k) \cdot \alpha_1(\theta) + w^a(x,s=s_2,z,t=t_k) \cdot \alpha_2(\theta) +$$

533 $$w^s(x,s=s_1,z,t=t_k) \cdot \beta_1(s) + w^s(x,s=s_2,z,t=t_k) \cdot \beta_2(s)$$

(7)

534

with 1 and 2 indicating sections A and B respectively. Note that Eq. (7) provides an analytical

535 expression for the water content in any point of the embankment at the discrete time points t_k.

536 So, provided that sufficiently small space intervals between instrumented cross-sections are

537 employed and sufficiently small time intervals are used, the water content in the embankment

538 could, in principle, be monitored as accurately as desired. So, one may be tempted to

539 conclude that the use of the geotechnical suite alone is good enough for the health monitoring

540 of the embankment. However, maintenance costs of the geotechnical suite over the typical

541 lifespan of flood defence earth embankments (at least 50 years but more often 100-200 years)

542 are higher than the costs for a monitoring programme based on geophysical measurements

543 which only entail non-invasive periodic walk-over surveys. More importantly, only two

544 sections have been used here. With regards to this point, in the authors' opinion, the proposed

545 geotechnical suite may be employed as the only monitoring method, but in order to obtain

546 accurate results, many more sections in the embankment should be monitored. If only a few

547 sections are employed to keep the monitoring costs within affordable limits, geophysical

548 probes are necessary to integrate the discrete geotechnical data with spatially continuous

549 measurements acquired along the entire embankment. Such a procedure is detailed below.

550

551 **7.2 Integration of the geophysical data with the geotechnical suite**

552 Herein the variable σ will be employed to represent the ground electrical conductivity which

553 is a function of both space and time, hence $\sigma = \sigma(x,s,z,t)$. However, electromagnetic

554 probes provide a measure of σ which is averaged over a prismatic volume of ground where

555 the induced electrical field is non-zero. Considering a generic cross-section of the

556 embankment, we define:

557 $$\bar{\sigma}(s,t) = \frac{\int\limits_{A_{CMD}} w(x,s,z,t)dxdz}{A_{CMD}} \qquad (8)$$

558 with $A_{CMD} = b \cdot d$, b being the distance between the two ends of the electromagnetic probe

559 (hence corresponding to the width of the portion of the embankment cross-section where the

560 induced electrical field is non-zero) and d the so-called effective depth, *i.e.* the depth of the

561 induced electromagnetic field. Note that A_{CMD} is independent of the cross-section considered,

562 *i.e.* its size does not vary with s, but depends on the type of electromagnetic probe employed

563 (for this reason we called it A_{CMD}). The effective depth is a function of the type of ground and

564 of the vertical distance from the portable device to ground level. d is an unknown that we

565 determined by trial and error selecting the value which provides the best correlation between

566 electrical conductivity and water content as illustrated later on (see Figure 14).

567 In Figure 13a, the measurements taken by the CMD-2 device at six time points along

568 the entire embankment, $\bar{\sigma}_k(s) = \bar{\sigma}(s,t=t_k)$, are shown. It emerges that the shape of the

569 curves is approximately the same for all the times considered. Now let us introduce the

570 spatial average of $\bar{\sigma}(s,t)$ over the entire embankment length as:

571 $$\bar{\bar{\sigma}}(t) = \frac{\int\limits_{s=0}^{s=L} \bar{\sigma}(s,t)ds}{L} \qquad (9)$$

572   with the second above score bar denoting the spatial average over the longitudinal coordinate

573   s. Then, we can introduce the normalised cross-sectional average electrical conductivity as:

574    $$\bar{\sigma}_0(s,t) = \frac{\bar{\sigma}(s,t)}{\bar{\bar{\sigma}}(t)} \tag{10}$$

575   The normalised measurements taken at times t_k, *i.e.* $\bar{\sigma}_{0_k} = \bar{\sigma}_0(s,t=t_k)$, are plotted in Figure

576   13b. From the figure, it emerges that the curves coincide almost perfectly. This leads to

577   consider the average of $\bar{\sigma}_{0_k} = \bar{\sigma}_0(s,t=t_k)$ over time:

578    $$\underline{\bar{\sigma}}_0(s) = \underset{k}{average}\,\bar{\sigma}_0(s,t=t_k) = \underset{k}{average}\left(\frac{\bar{\sigma}(s,t=t_k)}{\bar{\bar{\sigma}}(t=t_k)} \right) \tag{11}$$

579   as the representative curve of the conductivity of the embankment. Note that herein the

580   underscore bar denotes time average. The measurements were taken by an operator walking

581   above the centre of the embankment horizontal upper surface. Therefore, they cannot detect

582   any conductivity variation due to different cross-section orientations, *i.e.* they are

583   independent of the angle θ. The time-independent function $\underline{\bar{\sigma}}_0(s)$ can be thought of as a

584   unique identifier of the embankment expressing the variation of conductivity along the s

585   coordinate due to the variation of geometrical, hydraulic and lithological properties of cross-

586   sections and to the effects of exposure to weather conditions independent of cross-section

587   orientation, *i.e.* cross-sectionally symmetric. On the other hand, the function $\bar{\bar{\sigma}}(t)$ reflects the

588   temporal effect of climatic variations (e.g. rainfall, wind, temperature variations, etc.) and

589   aging on the ground conductivity.

590

a)   b)
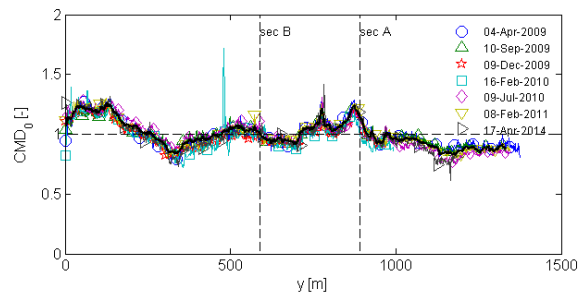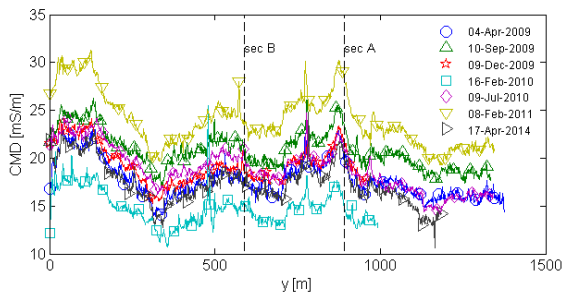
Figure 13. (a) electrical conductivity measurements along the embankments at seven different times; (b)
normalised values of conductivity measurements.

Now, we can split the ground conductivity function, $\bar{\sigma}(s,t)$, into the product of the time independent dimensionless function $\underline{\bar{\sigma}}_0(s)$ with the space independent dimensional function $\bar{\bar{\sigma}}(t)$:

$$\bar{\sigma}(s,t) = \underline{\bar{\sigma}}_0(s) \cdot \bar{\bar{\sigma}}(t) \qquad (12).$$

In the following it will be shown that this split is a necessary step to find a correlation between water content and electrical conductivity. First, let us define the average water content in the portion of the embankment cross-sections where the electromagnetic field is non-zero, *i.e.* A_{CMD}:

$$\bar{w}(s,t) = \frac{\int\limits_{A_{CMD}} w(x,s,z,t)\,dxdz}{A_{CMD}} \qquad (13)$$

Analogously to $\bar{\sigma}(s,t)$, we can split $\bar{w}(s,t)$ into two functions: a time independent dimensionless function, $\underline{\bar{w}}_0(s)$, which accounts for the effect of cross-section orientation and position on the ground water content and the space independent dimensional function, $\bar{\bar{w}}(t)$, which accounts for the effect of climatic variations and aging on the ground water content:

$$\bar{w}(s,t) = \underline{\bar{w}}_0(s) \cdot \bar{\bar{w}}(t) \qquad (14).$$

$\bar{\bar{w}}(t)$ represents the spatial average of the water content on the cross-sectional area A_{CMD} and along the longitudinal coordinate s:

$$\bar{\bar{w}}(t) = \frac{\int\limits_0^L \frac{\int\limits_{A_{CMD}} \left[\sum\limits_{i=1}^N w^a(x,s=s_i,z,t) \cdot \alpha_i(\theta) + \sum\limits_{i=1}^N w^s(x,s=s_i,z,t) \cdot \beta_i(s) \right] dxdz}{A_{CMD}} ds}{L} \qquad (15)$$

32

612   To look for a correlation between the measured electrical conductivity and water content,

613   we shall consider the time dependent functions $\bar{\bar{w}}(t)$ and $\bar{\bar{\sigma}}(t)$. Before doing so, we need to

614   account for the strong dependency exhibited by the ground electrical conductivity on

615   temperature (Keller and Frischknecht, 1966). Recently Hayley et al., (2007) investigated this

616   dependency for a range of temperatures corresponding to our case (temperature varying

617   between 0 and 25 Celsius) on a glacial till finding a linear dependency of the type:

618     $$\sigma = \sigma_{25}\left[C(T-25)+1\right] \qquad (16)$$

619   with σ being the electrical conductivity measured at the temperature T and the constant

620   C=0.02. To account for the effect of temperature on the measured electrical conductivity, we

621   expressed all the measured values relative to the same reference temperature before

622   correlating them to the water content. As shown in (Hayley et al., 2007), manipulating Eq.

623   (16), the following expression for the calculation of σ relative to the chosen reference

624   temperature is obtained:

625     $$\sigma_{ref} = \sigma \frac{1+C\left(T_{ref}-25\right)}{1+C(T-25)} \qquad (17)$$

626   with σ_{ref} being the value of electrical conductivity relative to the reference temperature T_{ref}.

627   Here, we chose T_{ref}=15 Celsius to minimise the amount of temperature compensation.

628   Employing Eq. (17), we calculated σ_{ref} from the in-situ values of σ and T.

629   In Figure 14, the water content measured at the time points t_k, $\bar{\bar{w}}(t=t_k)$ is plotted against

630   the electrical conductivity measured at the same time points, $\bar{\bar{\sigma}}_{ref}(t=t_k)$. It emerges that the

631   relationship between $\bar{\bar{w}}(t)$ and $\bar{\bar{\sigma}}_{ref}(t)$ is well captured by a linear function so that:

632     $$\bar{\bar{w}}(t) = m\bar{\bar{\sigma}}_{ref}(t)+q \qquad (18)$$

633 with *m* and *q* determined by best fit (see Figure 14). Substituting Eq. (17) into Eq. (18), it

634 becomes:

635 $$\bar{\bar{w}}(t) = m\bar{\bar{\sigma}}(t)\frac{1+C\left(T_{ref}-25\right)}{1+C\left(T-25\right)}+q \qquad (19).$$

636 Eq. (19) links the in-situ measured water content to the in-situ measured electrical

637 conductivity.
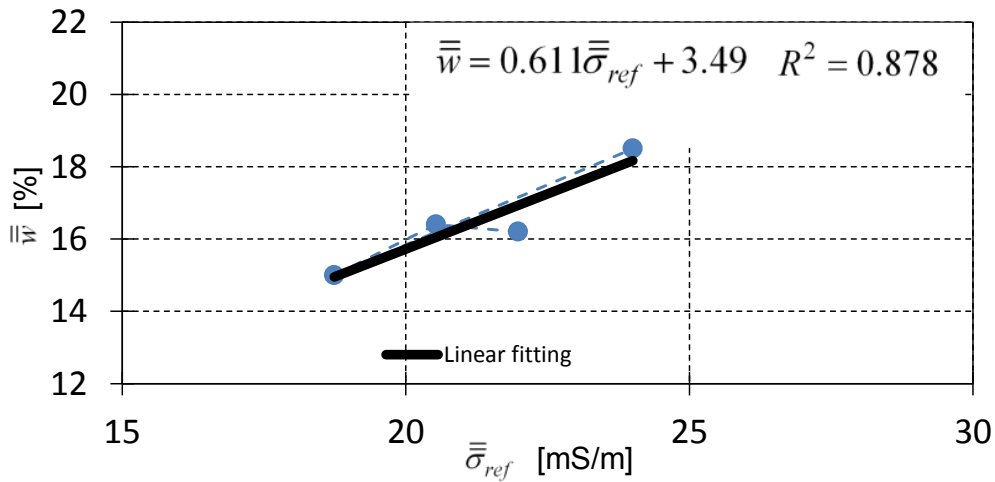
638

639 *Figure 14. Correlation obtained over the monitored 2 year time period between $\bar{\bar{\sigma}}_{ref}$, electrical conductivity at*
640 *the chosen reference temperature (T_{ref}=15°C), and $\bar{\bar{w}}$ calculated for an effective depth of d=0.2m.*

641

642   In order to work out the water content in any point of the embankment, $w(x,s,z,t)$, the

643 space independent dimensional function $\bar{\bar{w}}(t)$, must be multiplied by a normalised time

644 independent function, $\underline{w}_0(x,s,z)$, so that:

645 $$w(x,s,z,t) = \underline{w}_0(x,s,z)\cdot\bar{\bar{w}}(t) \qquad (20).$$

646 Following the approach adopted in par. 7.1, $w_0(x,s,z)$ is split into the summation of two

647 parts, an anti-symmetrical and a symmetrical one:

648 $$\underline{w}_0(x,s,z) = \underline{w}_0{}^a(x,s,z) + \underline{w}_0{}^s(x,s,z) \qquad (21)$$

34

649   As in par. 7.1, we assume $\underline{w}_0{}^a(x,s,z)$ to be the time average of the linear combination of the

650   functions expressing the normalised water content measured at times t_k at the N instrumented

651   cross-sections, $w_{0_{i;k}}{}^a(x,z)$:

652     $$\underline{w}_0{}^a(x,s,z) = \underset{k}{average}\left[\sum_{i=1}^{N} w_{0_{i;k}}{}^a(x,z)\cdot\alpha_i(\theta)\right] \qquad (22)$$

653   According to standard normalisation procedures, $w_{0_{i;k}}{}^a(x,z)$ and $w_{0_{i;k}}{}^s(x,z)$ are defined as:

654     $$w_{0_{i;k}}{}^a(x,z) = w_0{}^a(x,s=s_i,z,t=t_k) = \frac{w^a(x,s=s_i,z,t=t_k)}{\dfrac{\displaystyle\int_{A_i} w^a(x,s=s_i,z,t=t_k)dxdz}{A_i}}$$

655     $$w_{0_{i;k}}{}^s(x,z) = w_0{}^s(x,s=s_i,z,t=t_k) = \frac{w^s(x,s=s_i,z,t=t_k)}{\dfrac{\displaystyle\int_{A_i} w^s(x,s=s_i,z,t=t_k)dxdz}{A_i}} \qquad (23)$$

656   with A_i being the area of the ith cross section.

657   For the symmetrical function $\underline{w}_0{}^s(x,s,z)$, we assume the following expression:

658     $$\underline{w}_0{}^s(x,s,z) = \bar{w}^s(s,t)\cdot\bar{\sigma}_0(s) = \underset{k}{average}\left[\sum_{i=1}^{N} w_{0_{i;k}}{}^s(x,z)\cdot\beta_i(s)\right]\bar{\sigma}_0(s) \qquad (24).$$

659   The dimensionless function $\bar{\sigma}_0(s)$ accounts for the spatial variation of water content along

660   the longitudinal direction of the embankment detected by the geophysical probe during walk-

661   over surveys. Eq. (24) constitutes an important improvement in comparison with Eq. (4) since

662   the time average of the linear combination of the water content values measured at the N

663   instrumented cross sections, $\underset{k}{average}\left[\sum_{i=1}^{N} w_{0_{i;k}}{}^s(x,z)\cdot\beta_i(s)\right]$, is adjusted by multiplication with

664     $\bar{\sigma}_0(s)$ to account for the spatial variation of conductivity detected by the geophysical survey

665   along the longitudinal direction. The advantage of employing geophysics is now apparent

666   since it provides measurements which are continuous along the spatial coordinate s. This

667   allows improving the quality of the estimated water content especially in the zones of the

668   embankment farthest away from the geotechnically instrumented cross-sections.

669   So far the symmetrical component of the water content, $\underline{w}_0^s(x,s,z)$ has been related to

670   the geophysical measurements of the variation of ground electrical conductivity along the s

671   coordinate, *i.e.* dependent on cross-section position. In principle it should also be possible to

672   relate the anti-symmetrical component of the water content $\underline{w}_0^a(x,s,z)$ to geophysical

673   measurements of the variation of ground electrical conductivity due to cross-section

674   orientation, *i.e.* dependent on the angle θ. Let us recall that the geophysical measurements

675   were taken by an operator walking above the centre of the embankment horizontal upper

676   surface where the effect of cross-section orientation is negligible so that the measurements

677   are a function of cross-section position only (hence of the s coordinate only). To correlate

678   electrical conductivity to the anti-symmetrical part of the water content, measurements of

679   electrical conductivity along more than one path would be needed with some of them being

680   along the embankment flanks. However, these measurements would be likely affected by a

681   large error since it is very difficult to walk for long distances on the embankment flanks

682   (which are variously inclined), keeping a constant geometrical height (z coordinate).

683   Now, substituting Eq. (19), (22) and (24) into Eq. (20), the water content at the time t_l of

684   the geophysical measurement $w(x,s,z,t=t_l)$, can be derived as a function of the average

685   cross-sectional ground conductivity, $\bar{\sigma}(s,t=t_l)$:

686
$$w(x,s,z,t=t_l) = \left\{ average\left[\sum_{i=1}^{N} w_0^a(x,s=s_i,z,t=t_k) \cdot \alpha_i(\theta) \right] + average_k\left[\sum_{i=1}^{N} w_0^s(x,s=s_i,z,t=t_k) \cdot \beta_i(s) \right] \cdot \bar{\underline{\sigma}}_0(s) \right\} \cdot$$

687
$$\cdot \left(m \frac{\bar{\sigma}(s,t=t_l)}{\bar{\underline{\sigma}}_0(s)} \frac{1 + C(T_{ref} - 25)}{1 + C(T - 25)} + q \right) \qquad (0).$$

688   Eq. (25) provides the analytical expression to be employed to monitor the water content in the

689   embankment carrying out periodic walk-over surveys over a time period which can be much

690   longer than the time of activity of the geotechnical suite (*i.e.* $t_l \, ? \quad t_k$).

691   The spatial distributions of the water content calculated using Eq. (25) in four cross-

692   sections (s = 2, 182, 672 and 972m) from the electrical conductivity profile of the

693   embankment, measured during a walk-over survey carried out on 17th April 2014 (so for

694    $t_l > t_k$), are plotted in Figure 15. In order to provide a validation of the proposed method, a

695   few soil samples were retrieved from the embankment and brought to the laboratory for

696   accurate measurement. In the plots of Figure 15*c* and *d*, the experimental values of water

697   content are reported as triangles. Comparing the predictions of the method with the

698   experimental measurements of water content, the predictions show to be in very good

699   agreement with the experimentally measured values. This is quite remarkable especially in

700   light of the fact that the measurements were taken at a time (17th April 2014) well beyond the

701   2 year period within which the geotechnical and geophysical measurements had been

702   performed to calibrate the model.

703

37
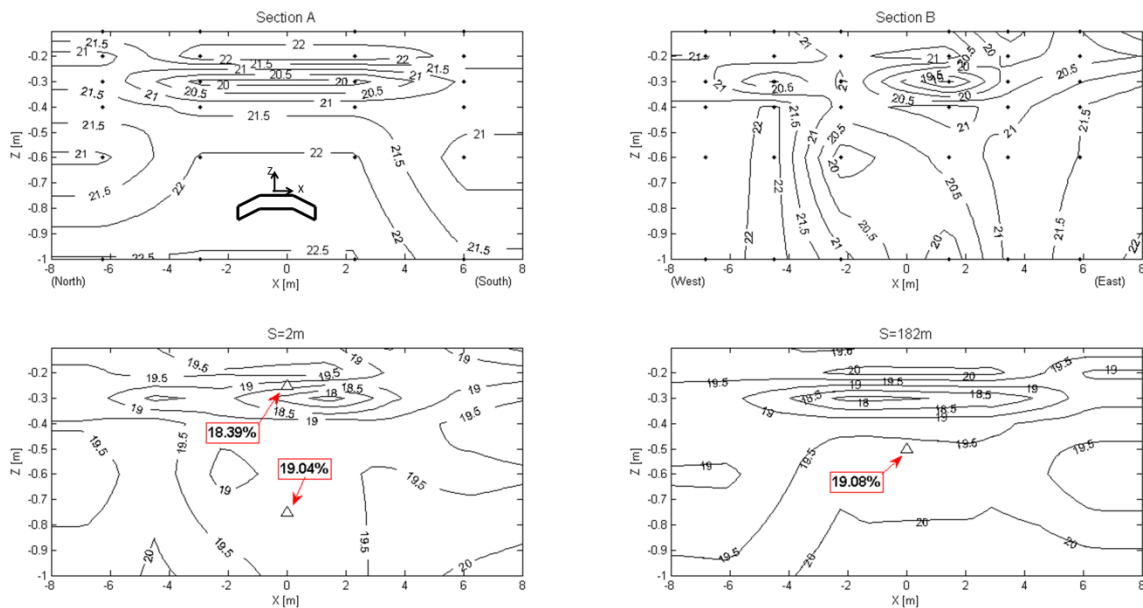
704 *Figure 15. values of the water content estimated from the electrical conductivity measured by the CMD-2 during*
705 *a walk over survey carried out on 17th April 2014 employing the proposed methodology . a) water content in*
706 *section A; b) water content in section B; c) water content at s=2m; d) water content at s=182.The triangles in*
707 *figures c) and d) indicate the value of water content measured in the laboratory from the retrieved in-situ*
708 *samples.*

709

710 **7.3 Options for long term monitoring**

711 In light of our results, three options of increasing accuracy but also requiring increasing costs

712 emerge for the monitoring of the embankment water content over time. The first and cheapest

713 option consists of using meteorological data only; the second more expensive option relies on

714 periodic walk-over surveys to retrieve geophysical data employing electromagnetic probes;

715 the third most expensive option requires both periodic walk-over surveys to retrieve

716 geophysical data and measurements in a number of cross-sections from a permanent

717 geotechnical suite. The first option requires the use of the geotechnical suite for an initial

718 limited period of time without any periodic (geotechnical or geophysical) measurement at

719 subsequent times. In the second option, the integration of geotechnical data with geophysical

720 ones (section 7.2) is carried out in a first limited initial period only whereas in the third option

721 it is carried out repeatedly during the whole lifetime of the structure. The second option

722 provides predictions more robust than the first one since the first option relies on a

723 relationship between meteorological data and variation of the water content established over

724 the initial time of monitoring which is expected to change over time with the ageing of the

725 structure. Depending on the importance of the structure and the available financial resources,

726 the authorities in charge of the maintenance of the embankments can select the most suitable

727 option.

728

8.   A proposal for a susceptibility index to desiccation fissuring

Here, a proposal for a susceptibility index for a failure mechanism that can be directly related to the presence of desiccation cracks is put forward. Cooling and Marsland, (1953), Marsland and Cooling, (1958) and more recently Morris et al., (2007) and Dyer et al., (2009) have described failure mechanisms which take place when water overflows the embankment crest in the presence of an interconnected pattern of vertical and horizontal cracks underneath the horizontal upper surface and the landward flank of the embankment. Overtopping water seeping downwards into the open cracks leads to the progressive uplift and removal of intact blocks of ground, first from the landward flank and subsequently from the horizontal upper surface. This failure mechanism is particularly dangerous since it leads to the development of a fast breach which can lead to quick flooding. The formation of extensive cracks is also detrimental for the structure since it favours internal piping.

Tests run by Tang et al., (2012) on clay samples of various shape show that after 4 wetting-drying cycles, the onset of cracks can be uniquely related to the value of the soil water content, *i.e.* it becomes independent of the wetting-drying history. In Costa et al. (2013), it is shown that once the water content in clayey soils lowers below a threshold value near the plastic limit, $w_{plastic}$, no additional cracks are formed. The determination of a threshold value of water content at which an interconnected network of cracks is formed and equally the determination of a critical threshold value for piping failure are challenging issues outside of the scope of this paper. Unsaturated soil mechanics and the formation of desiccation fissures in cohesive soils are topics of intense current research. Therefore, it is plausible to expect that in the future, with further results becoming available, it will be possible to establish a better susceptibility index based on less crude assumptions. The index here proposed has been conceived to provide a purely qualitative indication about which zones of the embankment are liable to fissuring; so it has not to be relied upon for

754 quantitative predictions on the level of hazard, or on the likelihood of failure in these zones.

755 Here, for sake of simplicity, we assumed this threshold to coincide with the plastic limit

756 ($w_{plastic}$) of the till. As a first approximation, we also assumed that the ground zones where the

757 water content is below the plastic limit are fissured so that the portion of cross section where

758 $w<w_{plastic}$ is considered fully fissured; whereas the portion where $w>w_{plastic}$ is considered

759 intact. The sought susceptibility index has to reflect how far a cross-section is from the

760 critical condition leading to failure. Hence, the index here proposed is defined as the ratio of

761 the sectional area where cracks have formed, A_{fis}, over the sectional area required for the

762 development of the considered failure mechanism, A_{Ω}:

763 $$I = \frac{A_{fis}}{A_{\Omega}} \text{ with } 0<I<1 \qquad (26)$$

764 The size of A_{Ω} is a property of the ground. In Dyer et al. (2009), a maximum characteristic

765 depth for the formation of an interconnected network of cracks 0.6 m deep was observed in

766 trial pits excavated in embankments made of glacial tills similar to the embankment

767 investigated in our paper. Therefore, a depth of 0.6 m was used to determine the sectional

768 domain employed for the calculation of A_{Ω} (see Figure 16a).

769 In Figure 16b, the function I(s) representing the value of the index along the

770 embankment, has been plotted for two different time points. It can be observed that in winter

771 the susceptibility index is nil (*i.e.* no fissuring is expected) in most of the embankment, apart

772 from two rather small zones where the index spikes up to 1. Conversely in summer, the index

773 assumes values larger than 0 in the whole embankment. Figure 16b is sufficient to identify

774 the zones of the embankment which are most in need of remedial measures. However, it may

775 be useful to define categories of risk for intervention protocols whereby the type of

776 intervention and its urgency are related to the established categories. Here, as an example,

777 three categories were established: no risk (green color) associated to 0<I<0.5, moderate risk

778   (yellow color) associated to 0.5<I<0.90, and high risk (red color) associated to 0.90<I<1. In

779   the zones classed as high risk (I>0.9), cracks were observed during both the winter and the

780   summer period (see Figure 16e). Also, the plots in Figure 16c and *d* provide a user-friendly

781   visualisation of the location of the most critical zones in the embankment.
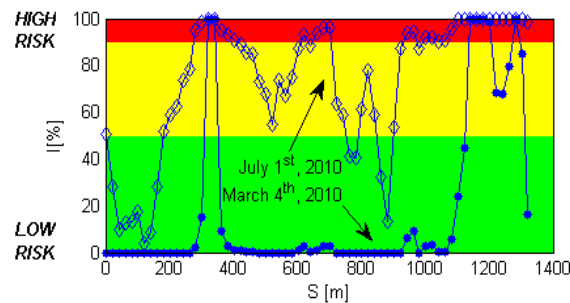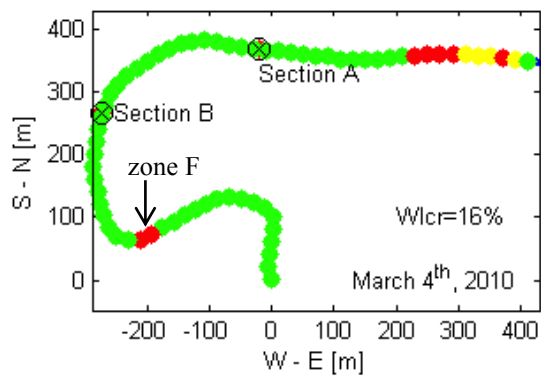
782
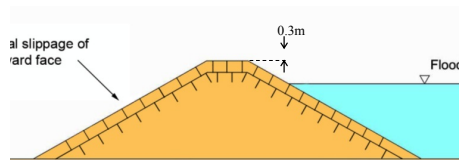
783

784   *a)*
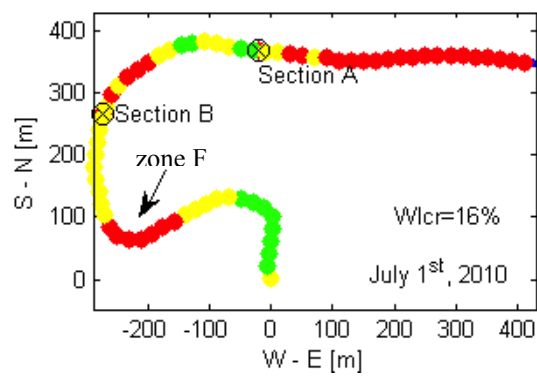

785

786   *b)*

787

788   *c)*   *d)*

789

790

791　*Figure 16. (a) representation of the total area A_Ω considered in the calculation of the susceptibility index (figure*
792　*modified from Dyer et al., 2009); (b) comparison between the calculated susceptibility index along the*
793　*embankment on March 4th and July 1st, 2010; (c) and (d) risk map of the embankment drawn on March 4th and*
794　*on July 1st, 2010; (e) picture of a surficial crack system taken in zone F of Figures c and d.*

795

9. Conclusions

797　In this paper, a cost effective methodology for the quantitative assessment of the potential for

798　desiccation fissuring for earthen embankments and tailing dams was established. Currently,

799　monitoring and condition assessment of embankments is performed by visual inspections at

800　set intervals. The proposed methodology is simple and suitable to be employed over the

801　entire lifetime of the structures by the authorities in charge of their maintenance. This

802　methodology paves the way for a radical improvement from the methods currently employed

803　moving to a quantitative assessment of the liability of long embankments (levees) to

804　desiccation fissuring.

805   The methodology is based on the use of a suite of standard geotechnical probes for the

806   measurement of the water content in a limited number of locations in the embankment

807   integrated with periodic non-invasive geophysical measurements from walkover surveys

808   employing portable electromagnetic probes. Most of the data from the geotechnical suite

809   were acquired by automatic reading systems involving minimal manpower. An innovative

810   calibration procedure was employed to calibrate the geotechnical probes (theta probe, profile

811   probe, diviner, etc.) in-situ by cross-comparison.

812   An index of susceptibility to desiccation induced deterioration was defined. Contour plots

813   of the calculated index provide an easy-to-be-used visual tool to monitor the health state of

814   the structure and identify the most critical zones to prioritise remedial interventions. Also a

815   protocol to monitor the susceptibility of earthen embankments to desiccation induced

816   deterioration over their lifespan is proposed based on three hierarchical levels of increasing

817   cost but also of increasing accuracy. The first and cheapest option consists of using

818   meteorological data only; the second more expensive option relies on periodic walk-over

819   surveys to retrieve geophysical data from the site; whereas the third most expensive option

820   requires both measurements in a number of cross-sections from a permanent geotechnical

821   suite and periodic walk-over surveys to retrieve geophysical data.

822

829   43

830	**Notation**	
831	i	integer indicating the number of the embankment cross section considered
832	k	integer indicating the chronological sequence of the measurement performed
833	m	slope coefficient for linear interpolation in Figure 14
834	q	intercept coefficient for linear interpolation in Figure 14
835	x	local Cartesian horizontal coordinate in the embankment cross-section
836	s	global curvilinear coordinate along the longitudinal axis of the embankment
837	s_t	local Cartesian coordinate orthogonal to x and z
838	z	local vertical downward Cartesian coordinate
839	P	vertical line (point on the embankment surface) in the cross section B of the embankment
840	X	global Cartesian coordinate
841	Y	global Cartesian coordinate
842	Z	global Cartesian coordinate
843	$w(x,s,z,t)$	water content
844	$w_{plastic}$	water content at the plastic limit
845	$w^s(x,s,z,t)$	symmetrical part of the cross-sectional water content
846	$w^a(x,s,z,t)$	anti-symmetrical part of the cross-sectional water content
847	$w_k = w(x,s,z,t=t_k)$	water content measured at the time t_k
848	$w_{i;k} = w(x,s=s_i,z,t=t_k)$	water content measured in cross-section i at time t_k
849	$w_P = w(x=x_P,s=s_P,z,t)$	water content measured along the vertical line P
850 851	$\bar{w}(s,t)$	cross-sectional water content average. The water content is averaged over the portion of embankment cross-section where the induced electric field is non zero (A_{CMD})

852 $\bar{\bar{w}}(t)$ space average of the water content (average over the entire embankment). The water content is

853   averaged over the portion of embankment cross-section where the induced electric field is non zero (A_{CMD})

854 $\bar{w}_0(s,t)$ normalised cross-sectional average water content

855 $\underline{\bar{w}}_0(s)$ time average of the normalised cross-sectional average water content

856 α weight function

857 β weight function

858 θ angle of s_t with the X axis. It indicates the orientation of a cross-section with regard to the global

859   Cartesian coordinate system

860 σ electrical conductivity

861 $\bar{\sigma}(s,t)$ cross-sectional average electrical conductivity. The electrical conductivity is averaged over the portion

862   of embankment cross-section where the induced electric field is non zero (A_{CMD})

863 $\bar{\sigma}_k(s) = \bar{\sigma}(s, t = t_k)$ cross-sectional electrical conductivity average measured at the time t_k

864 $\bar{\bar{\sigma}}(t)$ space average of the electrical conductivity (average over the entire embankment). The electrical

865   conductivity is averaged over the portion of embankment cross-section where the induced electric field is non

866   zero (A_{CMD})

867 $\bar{\sigma}_0(s,t)$ normalised cross-sectional average electrical conductivity.

868 $\underline{\bar{\sigma}}_0(s)$ time average of the normalised cross-sectional average electrical conductivity

869 A_{CMD} portion of cross-sectional area where the induced electric field is non-zero.

870 A_Ω portion of cross-sectional area with interconnected cracks causing a decrease of bearing capacity

871 A_{fis} portion of the cross-sectional area where $w < w_{plastic}$

872 A_i area of cross-section i

873 C   constant

874 I   susceptibility index

45

875

876   **References**

877   1. Allsop W., Kortenhaus A., Morris M., Buijs F., Hassan R., Young M., Doorn N., der Meer

878   J., Van Gelder P., Dyer M., Redaelli M., Utili S., Visser P., Bettess R., Lesniewska D.,

879   Horst W. (2007). Failure mechanisms for flood defence structures. EU FP7 FLOODSite

880   task 4, Research Report: T04-06-01.

881   2. Andersen G.R., Chouinard L.E., Bouvier C., Back W.E. (1999). Ranking procedure on

882   maintenance tasks for monitoring of embankment dams. *Journal of Geotechnical and*

883   *Geoenvironmental Engineering*, **125**, 247-259.

884   3. Aubeny C.P., Lytton R.L. (2004). Shallow slides in compacted high plasticity clay slopes.

885   *J Geotech & Geoenv Engrg ASCE*, **130**, 717-727.

886   4. Charles J.A. (2008). The engineering behaviour of fill materials: the use, misuse and

887   disuse of case histories. *Geotechnique*, **58**, 541-570.

888   5. Cooling L.F., Marsland A. (1953). Soil mechanics studies of failures in the sea defence

889   banks of Essex and Kent. *Proceedings of the ICE Conference on the North Sea Floods of*

890   *31 January/1 February 1953*, ICE, London, 58–73.

891   6. Costa S., Kodikara J., Shannon B. (2013). Salient factors controlling desiccation cracking

892   of clay in laboratory experiments. *Geotechnique*, **63**: 18-29.

893   7. D'Elisio C. (2007). Breaching of sea dikes initiated by wave overtopping: A tiered and

894   modular modeling approach. Ph.D. thesis, Univ. of Braunschweig, Germany, and Univ. of

895   Florence, Italy.

896   8. De Vita P., Di Maio R., Piegari E. (2012). A study of the correlation between electrical

897   resistivity and matric suction for unsaturated ash-fall pyroclastic soils in the Campania

898   region (southern Italy). *Environmental Earth Science*, DOI 10.1007/s12665-012-1531-4.

899   9. Di Maio R., Piegari E. (2011). Water storage mapping of pyroclastic covers through
900   electrical resistivity measurements. *Journal of Applied Geophysics* **75**, 196-202.

901   10. Dyer M., Utili S., Zielinski M. (2009). Field survey of desiccation fissuring of flood
902   embankments. *Proc. ICE Water Management* **162**, 221-232.

903   11. Environment Agency (2006). Condition assessment manual. Report DR 166_03_SD01

904   12. Gf Instruments (2011). Short guide for electromagnetic conductivity survey.
905   (www.gfinstruments.cz).

906   13. GID (2014). GID reference manual. Available at www.gidhome.com/support/manuals.

907   14. Hayley K., Bentley L.R., Gharibi M., Nightingale M. (2007). Low temperature
908   dependence of electrical resistivity: implications for near surface geophysical monitoring.
909   *Geophysical Research Letters*, **34**: L18402.

910   15. Keller G.V., Frischknecht F.C., (1966). *Electrical Methods in Geophysical Prospecting*.
911   Pergamon Press, Oxford, 517p.

912   16. Konrad JM., Ayad R. (1997). Desiccation of a sensitive clay: field observations. *Canadian
913   Geotechnical Journal*, **34**: 929–942.

914   17. Marsland A., Cooling L.F. (1958). Tests on Full Scale Clay Flood Bank to Study Seepage
915   and the Effects of Overtopping. Building Research Station, Watford, Internal report No.
916   C562.

917   18. Milly P., Wetherald R., Dunne K., Delworth T. (2002). Increasing risk of great floods in a
918   changing climate. *Nature*, **415**(6871), 514–517.

919   19. Morris M., Dyer M., Smith P., Falkingham J., Simms J. (2007). Management of Flood
920   Defences. Defra/EA, R&D report FD2411, London.

921   20. Munoz-Castelblanco J.A., Pereira J.M., Delage P., Cui Y.J. (2012a). The Influence of
922   Changes in Water Content on the Electrical Resistivity of a Natural Unsaturated Loess.
923   *Geotechnical Testing Journal*, **35**(1): 11-17.

924   21. Munoz-Castelblanco J.A., Pereira J.M., Delage P., Cui Y.J. (2012b). The water retention
925   properties of a natural unsaturated loess from northern France. *Geotechnique*, **62**, 95-106.

926   22. Perry J., Pedley M., Reid M. (2001). Infrastructure embankment: condition appraisal and
927   remedial treatment. CIRIA Report C550.

928   23. Rodriguez R., Sanchez M., Ledesma A., Lloret A. (2007) Experimental and numerical
929   analysis of desiccation of a mining waste. *Canadian Geotechnical Journal*, **44**(6): 644-
930   658.

931   24. Shin H., Santamarina JC. (2011). Desiccation cracks in saturated fine-grained soils:
932   particle level phenomena and effective stress analysis. *Geotechnique* **61,** 11, 961-972.

933   25. Smethurst J.A., Clarke D., Powrie W. (2012). Factors controlling the seasonal variation in
934   soil water content and pore water pressures within a lightly vegetated clay slope.
935   *Geotechnique*, **62**(5), 429-446.

936   26. Tang CS., Cui YJ., Shi B., Tang AM., Liu C. (2011). Desiccation and cracking behaviour
937   of clay layer from slurry state under wetting-drying cycles. *Geoderma*, **166**: 111-118.

938   27. Utili S. (2013). Investigation by limit analysis on the stability of slopes with cracks.
939   *Geotechnique*, **63**(2), 140-154.

940   28. Xu C.Y., Singh V.P. (2001). Evaluation and generalization of temperature-based methods
941   for calculating evaporation. *Hydrological Processes*, 15(2): 305-319.

942   29. Wan C.F., Fell R. (2004). Investigation of rate erosion of soils in embankment dams. *J. of
943   Geoenv. and Geotech. Engrg ASCE*, **130**, (4), 373-380.

944   30. Wu W. et al. (2011). Earthen embankment breaching. *Journal of Hydraulic Engineering
945   ASCE*, **137**, 1549-1564.

946   31. Zhang Z., Tao M., Morvant M. (2005). Cohesive slope surface failure and evaluation. *J*
947   *Geotech & Geoenv Engrg ASCE*, **131**, 898-906.

948   32. Zielinski M. (2009). Influence of desiccation fissuring on the stability of flood
949   embankments. PhD thesis, University of Strathclyde, Glasgow (UK).

950   33. Zielinski M., Sanchez M., Romero E., Sentenac P. (2011). Assessment of water retention
951   behaviour in compacted fills. *Proc. ICE Geotechnical Engineering*, **164**, 139-148.